Eur. Phys. J. A **28**, s01, 197–208 (2006)
DOI: 10.1140/epja/i2006-09-021-6

EPJ A direct
electronic only

X-ray phase contrast imaging at MAMI

M. El-Ghazaly[a], H. Backe, W. Lauth, G. Kube[b], P. Kunz, A. Sharafutdinov, and T. Weber

Institut für Kernphysik der Universität Mainz, D-55099 Mainz, Germany

/
Published online: 6 June 2006 – © Società Italiana di Fisica / Springer-Verlag 2006

Abstract. Experiments have been performed to explore the potential of the low emittance 855 MeV electron beam of the Mainz Microtron MAMI for imaging with coherent X-rays. Transition radiation from a micro-focused electron beam traversing a foil stack served as X-ray source with good transverse coherence. Refraction contrast radiographs of low absorbing materials, in particular polymer strings with diameters between 30 and 450 μm, were taken with a polychromatic transition radiation X-ray source with a spectral distribution in the energy range between 8 and about 40 keV. The electron beam spot size had standard deviation $\sigma_h = (8.6 \pm 0.1)\,\mu$m in the horizontal and $\sigma_v = (7.5 \pm 0.1)\,\mu$m in the vertical direction. X-ray films were used as detectors. The source-to-detector distance amounted to 11.4 m. The objects were placed in a distance of up to 6 m from the X-ray film. Holograms of strings were taken with a beam spot size $\sigma_v = (0.50 \pm 0.05)\,\mu$m in vertical direction, and a monochromatic X-ray beam of 6 keV energy. A good longitudinal coherence has been obtained by the (111) reflection of a flat silicon single crystal in Bragg geometry. It has been demonstrated that a direct exposure CCD chip with a pixel size of $13 \times 13\,\mu$m^2 provides a highly efficient on-line detector. Contrast images can easily be generated with a complete elimination of all parasitic background. The on-line capability allows a minimization of the beam spot size by observing the smallest visible interference fringe spacings or the number of visible fringes. It has been demonstrated that X-ray films are also very useful detectors. The main advantage in comparison with the direct exposure CCD chip is the resolution. For the Structurix D3 (Agfa) X-ray film the standard deviation of the resolution was measured to be $\sigma_f = (1.2 \pm 0.4)\,\mu$m, which is about a factor of 6 better than for the direct exposure CCD chip. With the small effective X-ray spot size in vertical direction of $\sigma_v = (1.2 \pm 0.3)\,\mu$m and a geometrical magnification of up to 7.4 high-quality holograms of tiny transparent strings were taken in which the holographic information is contained in up to 18 interference fringes.

PACS. 87.59.Bh X-ray radiography – 52.59.Px Hard X-ray sources – 41.50.+h X-ray beams and X-ray optics – 07.85.Fv X- and gamma-ray sources, mirrors, gratings, and detectors – 07.85.Nc X-ray and gamma-ray spectrometers

1 Introduction

The contrast in conventional absorption X-ray imaging is based on the difference in the absorption of the materials constituting the sample. Thin samples of light elements, such as soft tissues and organic materials with $Z \leq 8$, show a weak absorption contrast even at low X-ray energies, *i.e.*, the big deficiency is that the conventional absorption radiography cannot distinguish between materials with similar attenuation coefficients. For low-Z materials, however, a high contrast could be obtained if the phase shift of the X-rays introduced by the object could be exploited instead of the intensity of the transmitted wave. The enhancement of the contrast is attributed to the fact that, in particular for low-Z materials, the phase shift for X-rays is higher than the absorption of the incident X-rays. Also, for the radiography based on the phase shift mechanism, the absorbed dose is considerably lower in comparison to the conventional absorption radiography, see, *e.g.*, refs. [1,2,3].

X-ray phase contrast imaging can be carried out with various methods, for an overview see the recent ref. [4]. In particular, it has been pointed out by Wilkins *et al.* [5] that a very simple experimental setup with a polychromatic X-ray source of good transverse coherence, *i.e.* a small micro-focused spot, is already sufficient. Information can be supplied by such a method on the sample morphology, *i.e.* its boundaries, interfaces and location of small features, see *e.g.* ref. [6,7,8]. If, in addition, the X-ray source emits monochromatic X-rays, holograms can be taken. The experimental setup is similar to that of Gabor in-line holography [9]. In principle, such a setup

[a] *Former PhD Scholarship Holder in the Long Term Mission System from the Arabic Republic of Egypt.*
[b] *Present address*: Deutsches Elektronen-Synchrotron DESY, Notkestraße 85, D-22603 Hamburg, Germany.

is rather simple but a highly transverse and longitudinal coherent X-ray source of good intensity and also high spatial resolution detectors are required. Such sources are available at third generation synchrotron radiation sources like ESRF, APS, and SPRING8, and hard X-ray phase contrast imaging, in-line holography and microtomography have been accomplished at these facilities, see, *e.g.*, refs. [10,11,12].

The work presented here exploits the potential of the low-emittance 855 MeV electron beam of the race track microtron MAMI to produce X-rays with very good transverse coherence. Our approach is based on transition radiation (TR) production in the X-ray region with a micro-focused electron beam. In sect. 2 some features of the complex refraction index will be recalled with particular view on phase contrast methods. In sect. 3 the results of phase contrast imaging with a polymonochromatic X-ray beam from a TR foil stack with good transverse coherence will be presented. Section 4 deals with our approach toward a hard X-ray in-line holography using monochromatic X-rays. The paper closes with a conclusion.

2 Absorption versus phase shift

When a parallel beam of X-rays penetrates matter, it suffers an attenuation and a phase shift. These macroscopic quantities are described by the complex refraction index of X-rays [13]

$$n(\omega) = 1 - \delta(\omega) + i\beta(\omega)\,. \tag{1}$$

The real part $\Re[n(\omega)] = 1 - \delta(\omega)$ describes the refraction of the wave of angular frequency ω in a material, the quantity $\delta(\omega)$ gives the deviation of the refractive index of a material from unity (refraction index of vacuum). It is called the refractive index decrement. The imaginary part $\Im[n(\omega)] = \beta(\omega)$ specifies the attenuation of the X-rays in matter. It is called the absorption index.

The transmission of an electromagnetic wave through a piece of matter of thickness d is illustrated schematically in fig. 1. The undisturbed wave propagation in x-direction is described by the expression

$$A_v = A_0 e^{i(k_v d - \omega t)}; \quad k_v = \frac{\omega}{c}\,. \tag{2}$$

The amplitude of the outgoing wave behind the object is

$$A_m = A_0 e^{i(k_m d - \omega t)} = A_0 e^{-i\frac{\omega}{c}\delta\cdot d} e^{-\frac{\omega}{c}\beta\cdot d} e^{i(k_v d - \omega t)}, \tag{3}$$

where $k_m = n\omega/c$ is the wave number in the medium. Equation (3) contains a phase factor $\exp(-i\phi(d))$ with $\phi(d) = \phi_m(d) - \phi_v(d) = (\omega/c)\delta \cdot d$ the phase difference between the wave in matter with phase ϕ_m, and in vacuum with phase ϕ_v. In addition, the wave suffers an amplitude attenuation $|A_m|/|A_v| = \exp[-(\omega/c)\cdot\beta\cdot d]$.

The ratio δ/β is drastically larger for a low-Z material in comparison with a high-Z material at photon energies in the order of 20–40 keV. For example, at a photon energy

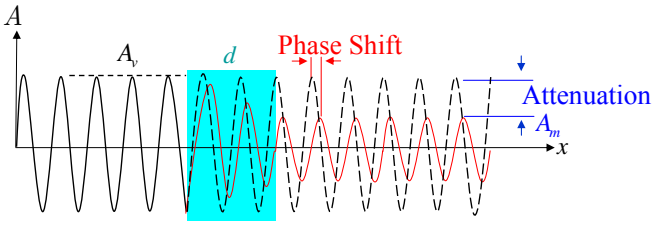

Fig. 1. Transmission of an electromagnetic wave through a piece of matter of thickness d and complex refraction index $n = 1-\delta+i\beta$. The transmitted wave is attenuated by the factor $\exp[-(\omega/c)\cdot\beta\cdot d]$ and has suffered a phase shift $\phi_m(d)-\phi_v(d) = (\omega/c)\cdot\delta\cdot d$ with respect to the unperturbed vacuum wave.

$\hbar\omega = 30$ keV, δ/β for polycarbonate ($C_{14}H_{14}O_3$) is approximately 40 times larger than for nickel ($Z \simeq 28$). This clearly demonstrates that for low-absorbing materials the phase shift dominates in comparison with the attenuation. For a polycarbonate foil of 10 μm thickness and a photon energy $\hbar\omega = 12$ keV, for which the complex refraction index parameters are $\delta = 1.826\cdot10^{-6}$ and $\beta = 1.573\cdot10^{-9}$, the phase shift is $\phi = 1.11$ rad while the intensity attenuation is only $1 - \exp[(-2\omega/c)\cdot\beta\cdot d] = 1.91\cdot10^{-3}$. These considerations lead to the important conclusion that a high contrast combined with a low absorbed dose could be achieved by using the phase shift mechanism to produce a radiograph [5]. In the next section the question will be addressed how the phase shift can be exploited for radiography.

3 Refraction contrast radiography

3.1 Basics

In an ideal experiment a point source emanates a monochromatic wave and illuminates the sample. The X-ray wavefront impinging on a sample will be deformed at the passage through the medium when its thickness or refractive index is inhomogeneous. In the framework of the eikonal approximation the wave vectors of the X-rays are normal to the equi-phase surfaces. In this picture of ray optics, *i.e.* for $\lambda \to 0$, the deviation from the initial direction is due to refraction.

For the sake of simplicity, in fig. 2 a one-dimensional object such as a string of radius R and a homogeneous refraction index $n_2 = 1 - \delta_2 + i\beta_2$ is considered, which is embedded in a medium of refraction index $n_1 = 1 - \delta_1 + i\beta_1$. It is illuminated with a nearly parallel X-ray beam. The phase shift of the outgoing wave relative to the wave in vacuum is given by

$$\phi(z_0) = \frac{4\pi}{\lambda}(\delta_2 - \delta_1)R\sqrt{1 - \left(\frac{z_o}{R}\right)^2}\,, \tag{4}$$

with z_o the vertical coordinate at the object. The angular deviation α of the normal to the incoming wavefront is, in the eikonal approximation,

$$\alpha = \frac{\lambda}{2\pi}\left|\frac{\partial\phi(z_0)}{\partial z_o}\right| = \frac{2(\delta_2 - \delta_1)}{R}\frac{z_o}{[1 - (\frac{z_o}{R})^2]^{\frac{1}{2}}}\,. \tag{5}$$

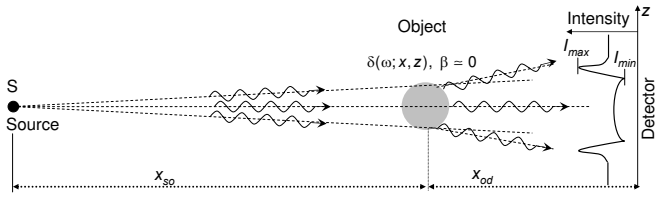

Fig. 2. Formation of a refraction contrast radiograph according to geometrical ray optics. Refracted X-rays slightly deviate from the initial propagation direction at the interfaces in accordance with Snell's law of refraction. Since the refraction index for X-rays is slightly smaller than unity (about 10^{-6}), X-rays are refracted in opposite manner to visible light, *i.e.* they are focused by a concave and defocused by a convex object. For tangentially incidence the X-rays encounter maximum deviation resulting in the formation of a contrast which enhances the visibility of the interfaces. The source-to-object distance is x_{so}, the object-to-detector distance x_{od} and the source-to-detector distance $x_{sd} = x_{so} + x_{od}$.

The phase gradient diverges at $z_o = R$. The rays deviate by a large angle from the original propagation direction even though $(\delta_2 - \delta_1)$ is very small as in the case of X-rays, which leads to a loss of intensity at boundaries or an edge contrast. This explains why the radiograph looks like a direct image of contours of the details which constitute the sample. More generally, any rapid variation of the refraction index or the thickness of the sample may be imaged by the edge contrast which appears in the radiograph even when a polychromatic X-ray beam is used.

In fact, the wave refracted by the sample interferes with the unperturbed wave. The diffracted wave and the unscattered wave form an interference pattern at the detector which is called a hologram. It is recorded by an image detector of high spatial resolution. For the polymer string with circular cross-section stretched along the horizontal y_o-axis, the normalized electric wave field $E(z_d, \lambda)/E_0(z_d, \lambda)$ at the detector plane can be calculated by means of the Fresnel-Kirchhoff integral. As shown in [14,15] the result is

$$\frac{E(z_d,\lambda)}{E_0(z_d,\lambda)} = 1 + \sqrt{\frac{x_{sd}}{i\lambda x_{so} x_{od}}} \cdot \int_{-R}^{+R} \left(\exp\left[-\frac{4\pi}{\lambda}(i\delta+\beta)\cdot R \cdot \sqrt{1-\frac{z_o^2}{R^2}}\ \right] - 1 \right) \cdot \exp\left[i\frac{\pi}{\lambda}\frac{x_{sd}}{x_{so}x_{od}}(z_o - z_d\frac{x_{so}}{x_{sd}})^2 \right] \mathrm{d}z_o \,. \tag{6}$$

The quantities x_{so}, x_{od}, and x_{sd} are defined in fig. 2. The normalized intensity distribution perpendicular to the string direction, the z_d-direction at the detector plane, $I_n^{(\delta)}(z_d, \lambda_0) = |E(z_d, \lambda_0)|^2/|E_0(z_d, \lambda_0)|^2$ is shown in fig. 3 (a) for a monochromatic X-ray source with wavelength λ_0. In a real experiment the spectral distribution of the X-rays and the finite beam spot size deteriorate

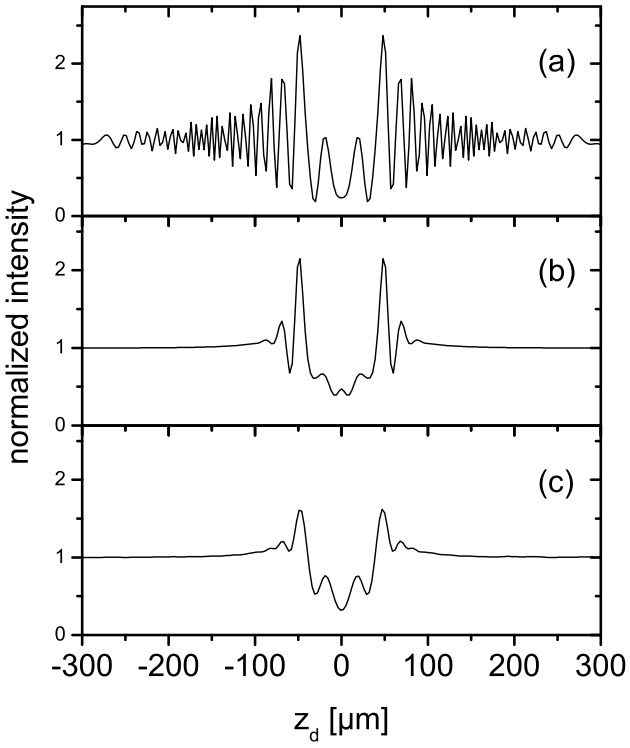

Fig. 3. Calculated interference patterns for a polymer string with a diameter of 30 μm, complex refraction index $\delta = 7.24 \cdot 10^{-6}$ and $\beta = 2.42 \cdot 10^{-8}$ at an X-ray energy of 6 keV, source-to-object distance $x_{so} = 10.45$ m, object-to-detector distance $x_{od} = 3.15$ m. (a) Normalized intensity distribution $|E(z_d, \lambda_0)|^2/|E_0(z_d, \lambda_0)|^2$ derived from eq. (6) for a point source and monochromatic X-rays with $\lambda_0 = 2.067$ Å, corresponding to an energy of 6 keV; (b) for a point source but a Gaussian spectral distribution around λ_0 with standard deviation of $\sigma_\lambda = 0.6$ Å; (c) for a Gaussian intensity distribution of the X-ray source spot with standard deviation $\sigma_z = 6\,\mu$m and monochromatic X-rays. Convolutions according to eq. (7). Ideal detector resolution is assumed.

the visibility of the interference fringes as demonstrated in fig. 3 (b) and (c). Source spot size and spectral distribution have been taken into account as convolutions with the normalized intensity distributions $g(z_s)$ of the beam spot and the spectral distribution $f(\lambda)$ of the X-rays according to

$$I_n(z_d) = \iint I_n^{(\delta)}\left(z_d - \frac{x_{od}}{x_{so}} z_s, \lambda - \lambda_0 \right) \cdot g(z_s) \cdot f(\lambda) \cdot \mathrm{d}z_s \cdot \mathrm{d}\lambda \,. \tag{7}$$

It can be seen from fig. 3 (b) that a few interference fringes remain visible, which resemble the structure of the string, even for polychromatic X-rays with a small longitudinal coherence length $L_L = \lambda^2/(2\Delta\lambda) \approx \lambda$, and/or a beam spot size $\sigma_z = 6\,\mu$m (rms) which corresponds to a transverse coherence length $L_T = x_{sd} \cdot \lambda/(2\pi\sigma_z) = 75\,\mu$m. Radiography based on these conditions will be called in the following refraction contrast radiography. For X-ray in-line holography, both a very good transverse coherence and a good longitudinal coherence of the X-ray beam are required since the holographic information is imprinted in the interference pattern as shown in fig. 3 (a).

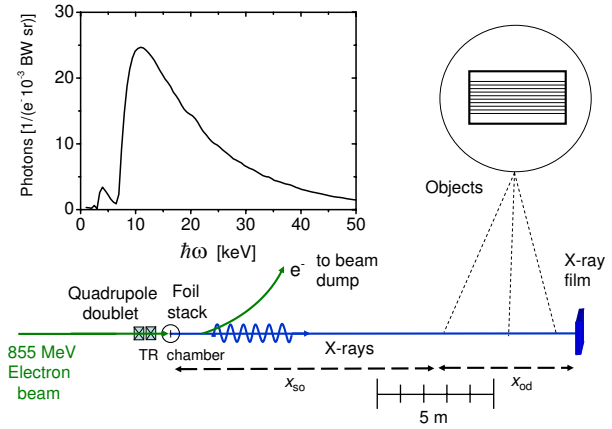

Fig. 4. Schematic diagram showing the experimental setup for refraction contrast radiography. The inset shows the calculated TR spectrum as function of the photon energy for which multiple scattering, electron beam divergence (0.6 mrad) and self absorption were taken into account. The foil stack consists of 30 polyimide foils with a thickness of 25 μm each, and spacings between the foils of 75 μm. It was optimized for a photon energy of 33 keV.

3.2 Experimental

The principle of the refraction contrast radiography will be explained by means of fig. 4. The 855 MeV electron beam, with a Lorentz factor $\gamma = 1673$, produces in a transition radiation foil stack a polychromatic X-ray beam which propagates in the forward direction in a cone with a typical apex angle of $2/\gamma \simeq 1.2$ mrad. The X-ray emission spectrum is shown in the inset of fig. 4. The polychromatic X-rays leave the vacuum system through a polyimide exit window of 120 μm thickness which is located at a distance of 5.88 m from the foil stack. The beam line is shielded by a concrete wall of 1 m thickness and 3.5 m height to reduce the background in the experimental area. The background originates from electrons which emitted a bremsstrahlung photon in the TR foil stack and left the beam line behind the bending magnet, as well as the background from the beam dump itself. The objects to be imaged are mounted in air at different distances from the target x_{so}, and from the X-ray film x_{od}, with $5.88\,\mathrm{m} < x_{so} < 13\,\mathrm{m}$ and $0\,\mathrm{m} < x_{od} < 7.12\,\mathrm{m}$, respectively. The source-to-detector distance was $x_{sd} = 11.38$ m.

The Mamoray MR5 II PQ X-ray film produced by Agfa[1] was used as position-sensitive detector. It is based on silver bromide with an emulsion thickness of $d_f = 12\,\mu$m [16]. The exposed X-ray films were processed manually. The X-ray films were digitized with a Nikon film scanner Super CoolScan 4000 ED [17] which has a spatial resolution of 4000 dpi [2] corresponding to a pixel size of $(6.35 \times 6.35)\,\mu\mathrm{m}^2$.

The primary quantity which is measured by an X-ray film is the photographic density D_p [18,16]. It is defined with the basis-10 logarithm as $D_p = \log(i_0/i)$ with i_0 the optical light intensity impinging on the film and i the intensity measured by the detector of the densitometer. From this primary quantity the so-called fog $D_f = \log(i_0/i_{0f})$ of an unexposed part of the film must be subtracted to obtain the density $D = D_p - D_f = \log(i_{0f}/i)$. The latter must be related to the exposure $b(\boldsymbol{r})$ of the film, *i.e.* the energy per unit area $\mathrm{d}E(\boldsymbol{r})/\mathrm{d}A$ deposited by the X-ray photons at a certain location $\boldsymbol{r}$ of the film.

In a simple theoretical model [18] the photographic density can be described by

$$D(\boldsymbol{r}) = D_{sat}(1 - \exp(-b(\boldsymbol{r})/b_0)) \; . \tag{8}$$

The saturation density D_{sat} and b_0 are characteristic quantities of the X-ray film. From eq. (8) the relative exposure is obtained as

$$\frac{b(\boldsymbol{r})}{b_0} = \ln\left(\frac{D_{sat}}{D_{sat} - D(\boldsymbol{r})}\right) \; . \tag{9}$$

Since we are interested in normalized exposure ratios $(b(\boldsymbol{r})/b_0)/(\overline{b}/b_0)$ with $\overline{b}$ the value without the object which can be replaced by a mean value on some position outside the domain of interest, the unknown quantity b_0 cancels. The still unknown saturation density D_{sat} must, in principle, be determined. However, since the digitization devices to our disposal had only a depths of 8 bits the main restriction in the dynamical range is expected to originate from the digitization procedure and not from the dynamical range of the X-ray film.

In view of the low digitization depth, the procedure we adapted to obtain the contrast C_{ref} of a string as defined by eq. (10) in the next subsection was the following. At first, domains on the X-ray film were selected in which the photographic density was assumed to be in the linear region. In this case eq. (8) reduces to $D(\boldsymbol{r}) = D_{sat} \cdot b(\boldsymbol{r})/b_0$ and in the exposure ratio also the saturation density cancels. Thereafter, we determined the contrast C_{ref} at various positions of the string for which the exposure varied due to the intensity profile of the X-ray beam spot and selected the maximum value as the experimental contrast.

3.3 Results

An extensive study of the contrast generation as a function of the object-to-detector distance x_{od} has been performed for polyamide strings of different diameters. Figure 5 (a) shows a typical example for a polyamide string [3] with a diameter of about 270 μm. The calculated absorption contrast for such a polyamide string does not exceed about 1%. Therefore, no absorption contrast can be observed with the traditional contact radiography, *i.e.* for $x_{od} \cong 0$, in accord with our measurements. By moving the object away from the detector, the imaging regime is changed from absorption radiography to phase contrast radiography and phase shift is the mechanism to produce the contrast. The contrast appears at the borders of the

[1] Agfa-Gevaert N.V., B2640 Mortsel Belgium.
[2] Dots per inch.
[3] Supplied by Goodfellow.

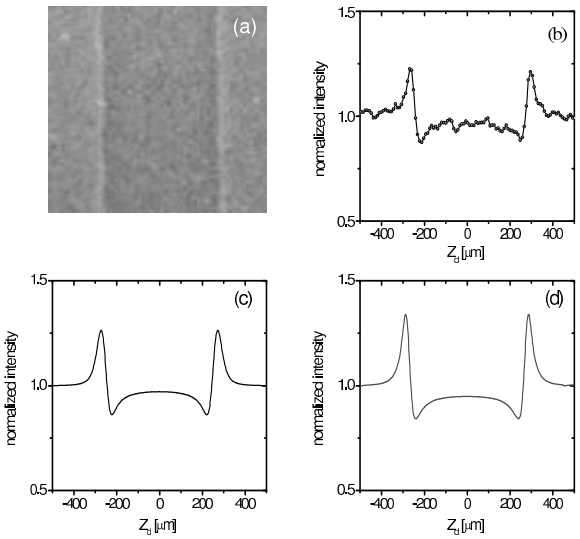

Fig. 5. Refraction-enhanced radiograph of a polyamide string with a diameter of 270 μm at an object-to-detector distance $x_{od} = 5.5$ m and a source-to-detector distance $x_{sd} = 11.38$ m. The electron beam current was 6 nA, the exposure time amounted to 60 s. X-ray source sizes were $\sigma_h = (8.6 \pm 0.1)\,\mu$m and $\sigma_v = (7.5 \pm 0.1)\,\mu$m in horizontal and vertical direction, respectively. (a) Radiograph, (b) intensity profile for which 100 vertical pixels were added together to improve the statistics. (c) Normalized intensity profile according to geometrical optics with the following parameters: film and scanner resolution $\sigma_t = (10.0 \pm 0.4)\,\mu$m, and the wave optical contribution $\sigma_w = \sqrt{\lambda x_{sd} x_{od}/(2\pi x_{so})} = 2.3\,\mu$m with $\lambda = 0.633$ Å. (d) Same as (c) on the basis of wave optics.

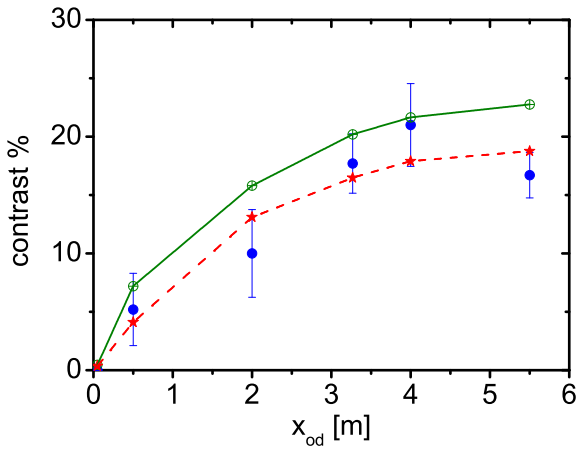

Fig. 6. Contrast C_{ref} for a polyamide string of 270 μm diameter as a function of the object-to-detector distance x_{od}. The source-to-detector distance $x_{so} = 11.38$ m was kept constant. Error bars are measurements, crossed circles calculations on the basis of the wave optical model with a beam spot size $\sigma_v = 7.5\,\mu$m and a total X-ray film resolution and scanner resolution $\sigma_t = (10.0 \pm 0.4)\,\mu$m. Stars designate calculations according to geometrical optics.

polyamide string where the density gradient reaches its maximum value. An edge contrast can be defined as

$$C_{ref} = \frac{I_{max} - I_{min}}{I_{max} + I_{min}} \tag{10}$$

with I_{max} and I_{min} defined in fig. 2. As can be seen from fig. 5 (b) the contrast amounts to $C_{ref} = 17.8\%$. The contrast C_{ref} as a function of the object-to-detector distance x_{od} is shown in fig. 6 as error bars for all measurements.

3.4 Discussion

The most interesting feature of the radiograph shown in fig. 5 is that an edge enhancement or phase contrast can be observed with a polychromatic X-ray beam. This fact has been discussed in a number of papers also in connection with the interplay between refraction and diffraction [5, 19]. The general features of refraction contrast imaging will be discussed by means of fig. 6. It can be stated that the distance x_{od} between object and detector must be at least as large that the wave optical spread of the diffracted X-rays becomes comparable with the detector resolution. Otherwise all interference fringes are blurred and the contrast is low. With increasing object-to-detector distance x_{od} the contrast increases about linearly. However, at the same time the projected X-ray spot size on the detector plane increases and this worsens the contrast at larger x_{od} distances. The maximum of the contrast is a function of the beam spot size and of the film resolution. But contrast is not the only figure of merit. It must also be taken into account that with increasing x_{od} the edge spread increases and the resolution deteriorates. The latter might be undesirable in case that resolution is of importance and nearby features must be resolved.

Next, the question will be addressed whether the measured edge enhancement structures can be understood quantitatively in the framework of the wave optical and geometrical models. As has already been pointed out above, the refraction contrast is in a strict sense a wave optical phenomenon, however, with some care it can also be explained in the framework of geometrical optics. Such an approach might be a good approximation at experimental conditions in which interference patterns are smeared out, *i.e.*, if the object is illuminated with polychromatic X-rays, or if the projected source size or the detector resolution are too large, respectively too bad. Both models have two free parameters which are the standard deviation of the beam spot size and the resolution of the X-ray film including the film scanner.

The wave optical calculations were performed with the effective X-ray spectrum which takes into account the transition radiation spectrum and the absorption characteristics of air and the X-ray film. The effective X-ray spectrum was approximated with 22 discrete values in the energy range between 8 and 30 keV. For the geometrical model it was sufficient to approximate the X-ray spectrum by a delta-function at the mean photon energy $\langle \hbar\omega \rangle = 19.6$ keV, corresponding to a wavelength $\lambda = 0.633$ Å, since model calculations showed, via the optical parameters, a rather weak energy dependence of the sharp edge structure. As can be seen, both the geometrical

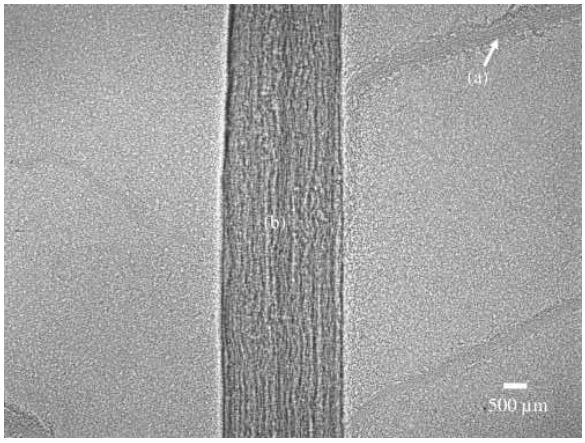

Fig. 7. A refraction contrast radiograph of a part of green leaf of *Rumex crispus*. The radiograph was recorded by the MAMORAY MR5 II PQ (Agfa) X-ray film. The object-to-detector distance was $x_{od} = 5.5\,\mathrm{m}$ at a source-to-object distance $x_{so} = 5.88\,\mathrm{m}$. With these parameters the magnification was 1.94 times. The electron beam energy was 855 MeV, the electron beam spot size had standard deviations of $\sigma_h = (8.6 \pm 0.1)\,\mu\mathrm{m}$ and $\sigma_v = (7.5 \pm 0.1)\,\mu\mathrm{m}$ in the horizontal and vertical direction, respectively. The TR foil stack described in fig. 4 was used. The electron beam current was 6 nA, the exposure time 40 s.

and the wave optical model describe the general features of the measurement quite well. The rather good results for the contrast ratio C_{ref} of the geometrical model, as shown for the example in fig. 5 (c), were obtained after a convolution with a Gaussian of standard deviation

$$\sigma = \sqrt{\left(\frac{x_{od}}{x_{so}}\right)^2 \sigma_s^2 + \sigma_d^2 + \sigma_p^2 + \frac{\lambda x_{od} x_{sd}}{2\pi x_{so}}}\,. \qquad (11)$$

This parameter takes into account projected source size σ_s, X-ray film resolution σ_d, pixel resolution of the film scanner σ_p, and an additional term $\sigma_w = \sqrt{\lambda x_{so} x_{od}/(2\pi x_{sd})}$. This term accounts for the diffraction which is absent in the geometrical model. It was estimated from the second exponential in eq. (6). The argument is that for a fixed point z_o at the object the typical spread in the detector plane is given by a region $|z_o x_{sd}/x_{so} - z_d| < \sigma_w$. For $|z_o x_{sd}/x_{so} - z_d| \gg \sigma_w$ the exponential oscillates rapidly and the mean value in z_d approaches zero. The real parameter σ_w may differ from the assumed one. However, the good agreement may be a consequence of the rather poor total film resolution $\sigma_t = \sqrt{\sigma_d^2 + \sigma_p^2} = 10\,\mu\mathrm{m}$ which is much larger as the wave optical contribution $\sigma_w = 2.3\,\mu\mathrm{m}$.

As an example of the visualization of low-Z objects by the refraction contrast, in fig. 7 the image of a green leaf is shown. In the part labelled with (a) where the leaf is thinner than 1 mm, the visibility of a bundle of vascular tissue (veins) could be resolved with high contrast. In the middle part labelled by (b), the object is about 3 mm thick and contains a bundle of vascular tissue (veins). However, the identification of an individual vein is difficult since images from the different veins in the radiograph are overlapping. Such three-dimensional structures may be disentangled by a holographic method some principles of which are sketched in the next section.

4 Toward hard X-ray in-line holography

In the preceding section it has been shown that the transition radiation (TR) X-ray source is well suited for refraction contrast imaging. This chapter deals with the investigation of the possibility of X-ray phase contrast imaging and hard X-ray in-line holography with monochromatic X-rays at MAMI. The good emittance of MAMI allows the preparation of a micro-focus which is a prerequisite of the required transverse coherence of the TR X-ray source. The longitudinal coherence can be achieved by a single-crystal monochromator. The basics of in-line holography, the experimental setup, the preparation of the micro-focused electron beam and the results obtained so far will be described in the following.

4.1 Basics

A wave emanating from a point source may illuminate an object from which it is scattered. The wave amplitude $E(\boldsymbol{r}) = E_0(\boldsymbol{r}) + E_{scat}(\boldsymbol{r})$ can be split into the reference wave $E_0(\boldsymbol{r})$ and a scattered wave $E_{scat}(\boldsymbol{r}) = a(\boldsymbol{r}) \cdot E_0(\boldsymbol{r})$. The amplitude ratio can be written as $E(\boldsymbol{r})/E_0(\boldsymbol{r}) = 1 + a(\boldsymbol{r})$. The scattering amplitude $a(\boldsymbol{r})$ contains the required information on the object. On a detector screen, such as an X-ray film or a CCD detector, the squared absolute values of the amplitudes $|E(\boldsymbol{r})|^2$ and $|E_0(\boldsymbol{r})|^2$ are measured from which the contrast image $|E(\boldsymbol{r})|^2 - |E_0(\boldsymbol{r})|^2$ can be obtained. By division through the reference wave $|E_0(\boldsymbol{r})|^2$ the normalized contrast ratio,

$$I_{norm}(\boldsymbol{r}) = \frac{|E(\boldsymbol{r})|^2 - |E_0(\boldsymbol{r})|^2}{|E_0(\boldsymbol{r})|^2} = 2\,\Re[a(\boldsymbol{r})] + |a(\boldsymbol{r})|^2, \qquad (12)$$

can be determined.

The appearance of $2\,\Re[a(\boldsymbol{r})] = a(\boldsymbol{r}) + a^*(\boldsymbol{r})$ on the right-hand side of eq. (12) shows that the hologram contains also information on the real part of the scattering amplitude rather than only its absolute value squared $|a(\boldsymbol{r})|^2$ which may be referred to as "classical diffraction pattern" of the complementary transmission function of the object [15]. Such classical diffraction patterns are observed in diffraction experiments in which the reference wave is absent, *e.g.*, at diffraction on a slit which is the complementary to an opaque object as, *e.g.*, an opaque wire. While the classical diffraction pattern is rather smooth, see fig. 8 (a), the holographic diffraction pattern oscillates rapidly, see fig. 8 (b). These oscillations have a rather small amplitude and can hardly be seen in a measurement of the hologram such is shown in fig. 8 (c). Much more pronounced oscillations are observed for transparent objects as polymer strings, see fig. 8 (d) and (e) which are maintained in the sum of the classical and the

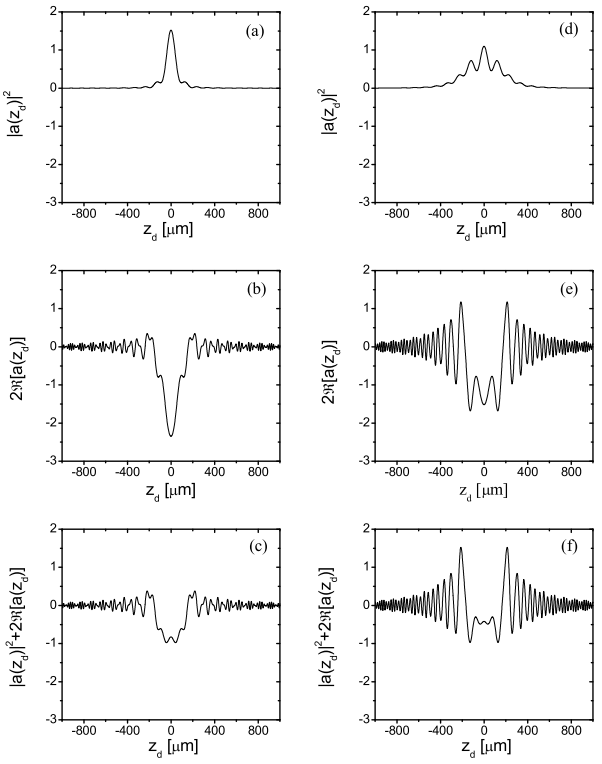

Fig. 8. Analysis of the calculated normalized contrast image in distinct patterns for a totally opaque tungsten wire, left column (a), (b) and (c), and for an approximately transparent polymer string, right column (d), (e) and (f). Both wires have the same diameter of 25 μm. The X-ray photon energy is 6 keV ($\lambda = 2.067$ Å), the complex refraction index parameters are $\delta_W = 8.5 \cdot 10^{-5}$ and $\beta_W = 1.1 \cdot 10^{-5}$ and $\delta_P = 7.3 \cdot 10^{-6}$ and $\beta_P = 2.55 \cdot 10^{-8}$ for tungsten and polymer, respectively, at this energy. The source-to-object distance is $x_{so} = 1.92$ m and the object-to-detector distance $x_{od} = 11.68$ m. Panels (a) and (d) show the classical diffraction pattern $|a(z_d)|^2$ which is the diffraction pattern of the complementary object, (b) and (e) show the holographic diffraction pattern $2\Re[a(z_d)]$ which come about by the interference between the wave front disturbed by the object and the reference wave emanating from the source, (c) and (f) show the normalized contrast images.

holographic diffraction pattern, see fig. 8 (f). These oscillations contain information on the distance between the object and the detector or the source, and via the refractive index decrement δ and the absorption β also on the bulk of the string. In addition, the hologram contains via the transverse coherence length also information on the beam spot size (ref. [20]).

4.2 Experimental

The observation of interference patterns as shown, for instance, in fig. 8 requires both, a good transverse and a good longitudinal coherence which can be achieved with a microfocused and monochromatic X-ray beam. These requirements led to an experimental arrangement at MAMI

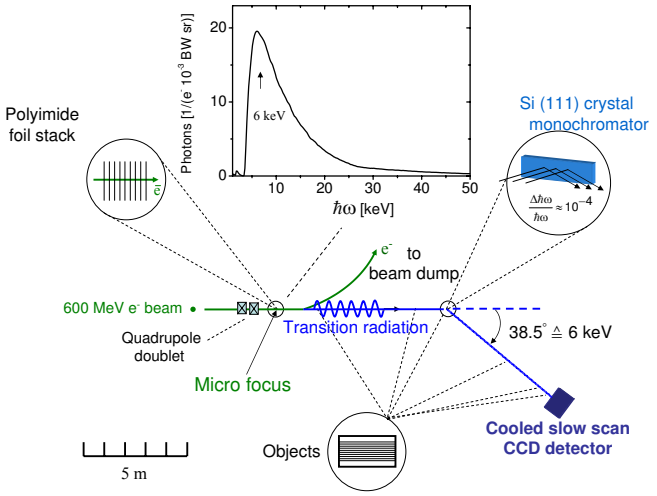

Fig. 9. Schematic experimental setup for X-ray in-line holography at MAMI. Shown are the TR foil stack, the single-crystal monochromator at a distance of 7.8 m from the target, and a CCD detector or an X-ray film at a distance of 5.8 m from the monochromator. The objects to be imaged can be positioned at distances of 1.88, 4.3, 7.47, 10.78, 12.71 and 13.6 m from the X-ray source. All components are housed in a connected vacuum system to avoid self-absorption of the X-rays. The inset shows the calculated TR energy spectrum as function of the photon energy for which multiple scattering, electron beam divergence (0.8 mrad) and self-absorption were taken into account. The TR foil stack consists of 25 polyimide foils with a thickness of 12.5 μm which are spaced out by aluminium foils of 100 μm thickness, the latter with centric holes of 2 mm diameter for the passage of the electron beam.

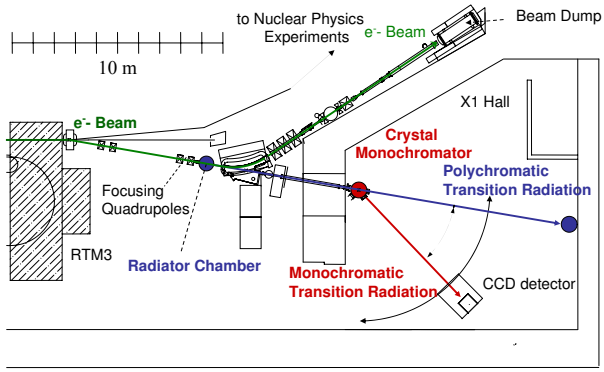

Fig. 10. Floor plan of the experimental area at MAMI. The electron beam is fed into the X1-beam line just behind the third stage of the race track microtron RTM3. During the course of the experiments the entrance to the X1 hall below is closed by a concrete door.

which is schematically depicted in fig. 9. The floor plan at MAMI is shown in fig. 10. A flat single crystal in Bragg geometry is used as monochromator. The objects to be imaged can be placed between the TR radiator and the monochromator crystal close to the TR source resulting in a magnification of the object of up to a factor of 7.4 or, alternatively, between monochromator and X-ray detector. The magnification may be of importance to compensate

for a moderate detector resolution if, *e.g.*, CCD-chips in a direct exposure mode are used, see below.

For the preparation of a micro-focused electron beam, a low beam emittance in horizontal and vertical directions is of particular importance. The emittance of the MAMI electron beam in horizonal direction is bigger than the emittance in vertical direction because the electrons emit synchrotron radiation in the bending magnets of race-track microtron 3. The horizontal emittance grows rapidly above an electron beam energy of 400 MeV, while the vertical emittance still decreases. As a compromise, a beam energy of 600 MeV was chosen for which the emittances are $\epsilon_h = 2.3\,\mu$m mrad and $\epsilon_v = 0.52\,\mu$m mrad in the horizontal and vertical directions, respectively.

The polyimide foil stack to produce transition radiation is optimized for a high X-ray flux at a photon energy of 6 keV at the electron beam energy of 600 MeV. The calculated photon energy spectrum is shown in the inset of fig. 9. The flat silicon single crystal with its surface parallel to the (111) crystal plane acts as a mirror for the TR photons. However, the mirror is energy dispersive in the horizontal direction. The deviation ε of the photon energy, defined by the equation $\hbar\omega = \hbar\omega_B(1+\varepsilon)$, from the nominal Bragg energy

$$\hbar\omega_B = \frac{2\pi\sqrt{h^2+k^2+l^2}}{a_0}\,\frac{\hbar c}{2\sin\theta_B} \tag{13}$$

is approximately given by the expression [21]

$$\varepsilon = \frac{\Re(\chi_0)}{2\sin^2\theta_B} - \frac{\theta_x}{\tan\theta_B}\,, \tag{14}$$

where $\theta_x = \theta - \theta_B$ is the deviation from the nominal Bragg angle θ_B. The integers h, k, l are the Miller indices, $a_0 = 5.4309$ Å the lattice constant, and $\Re(\chi_0)$ the real part of the dielectric susceptibility χ_0. The Bragg angle for $\hbar\omega_B = 6$ keV amounts for the (111) reflection to $\theta_B = 19.25°$.

In in-line holography a scattered wave from the object interferes with an unscattered wave from the source. For an assumed transverse coherence length of $L_T = 250\,\mu$m, at a distance of 13.6 m a $\theta_x = 18.4\,\mu$rad results. The angular spread which originates from the beam spot size and the pixel resolution is less than 1 μrad and can be neglected. The angle θ_x corresponds, according to eq. (14), to a relative energy shift of $5.3\cdot10^{-5}$ or $\Delta\hbar\omega = 0.32$ eV. This means that two waves with slightly different energies must interfere which is only possible if the longitudinal coherence length L_L is long enough. The width of the reflecting power ratio of the monochromator crystal is $\Delta\varepsilon = 1.4\cdot10^{-4}$ corresponding to $\Delta\hbar\omega = 0.84$ eV [21], and a longitudinal coherence length $L_L = 0.5\lambda^2/\Delta\lambda = 0.5\lambda/\Delta\varepsilon = 0.74\,\mu$m results. This value is sufficiently large for all objects investigated in this work which had thicknesses in the sub-mm range, since at a refractive index decrement of $\delta = 1\cdot10^{-6}$ the optical path difference is less than 0.01 μm.

Hard X-ray holography requires, like refraction contrast radiography, a two-dimensional resolving detector with a large dynamic range and linear relationship between the incident radiation intensity and the response of the detector. Such conditions can be fulfilled by a charge-coupled device (CCD) or an X-ray film. For the current experiments the CCD system ANDOR DO-434 BN CCD [22] was used. It contains a back-illuminated CCD low-noise sensor from Marconi CCD47-10 [23] with 1024×1024 pixels of size $13\times13\,\mu$m^2. The chip has a good quantum efficiency over a wide spectral range. For X-rays of 6 keV energy it amounts to still about 45%. These features offer the opportunity to use the CCD chip in the direct exposure mode in which the signal is generated by direct energy deposition of X-rays in the sensitive layer of approximately 10 μm thickness.

Direct-exposure CCD camera chips have, compared with X-ray films, the big advantage that they have a good linearity over a wide dynamical range, a good signal-to-noise ratio, and that they are on-line capable. The latter fact is very important since contrast or normalized contrast images can easily be generated in which all parasitic background, originating not from the object, can be eliminated. The disadvantage of a moderate spatial resolution in comparison to an X-ray film can be alleviated by a geometrical magnification. In reality, however, the spatial resolution is larger than the pixel size because of so-called split events in which the deposited energy is shared by neighboring pixels.

The Structurix D3 X-ray film from Agfa is a useful detector as well. The main advantage in comparison with the direct exposure CCD chip is its very good resolution. The standard deviation of the resolution was measured to be $\sigma_f = (1.2\pm0.4)\,\mu$m, which is about a factor of 6 better than for the direct-exposure CCD chip. The main disadvantage of the X-ray film is the missing on-line capability with the consequence that the generation of normalized contrast images is rather involved.

The procedure to obtain the intensity information from the photographic density is similar to that already described in sect. 3.2. The X-ray film was digitized with a film scanner (Nikon Coolscan LS 4000 [17]) and with an optical microscope equipped with a high-resolution 8-bit CCD camera (F-View XS [24]). From this system limitations are expected because the dynamical range cannot be better than the digitization depth of the ADC (1:256), while the X-ray film has a dynamical range which is more than a factor of 10 better (3.5 decades corresponding to 1:3160). Since, in addition, the illumination time was selected automatically by the scanner after the part of interest of the picture and the optical magnification were selected, the holograms were digitized at various positions of the string. Along the imaged strings the exposure is changing and the sector with the best contrast was selected for further analysis.

4.3 Measurements and discussion

4.3.1 Investigation of the transverse coherence in horizontal direction

To study the coherence in the horizontal and vertical directions, radiographs of two polymer strings of the same

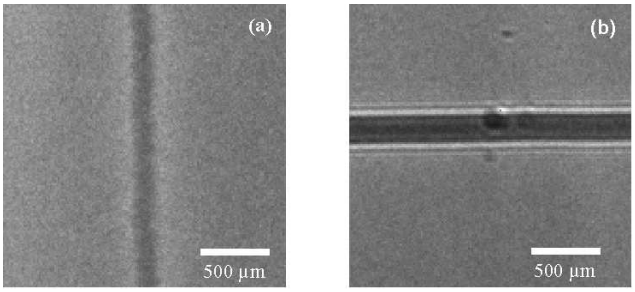

Fig. 11. Two radiographs of a polymer string of diameter 30 μm. In radiograph (a) the string is mounted vertically, in (b) horizontally. The X-ray source spot size was $\sigma_h = (1.7 \pm 0.1)\,\mu$m in the horizontal and $\sigma_v = (3.9 \pm 0.4)\,\mu$m in the vertical direction. The electron beam spot size was checked with the wire scanner before and after the imaging in order exclude a possible shift of the beam spot. The source-to-object distance was $x_{so} = 4.3$ m, and the object-to-detector distance $x_{od} = 9.61$ m. Electron beam current 700 nA, exposure time 1.8 s, 50 frames added up.

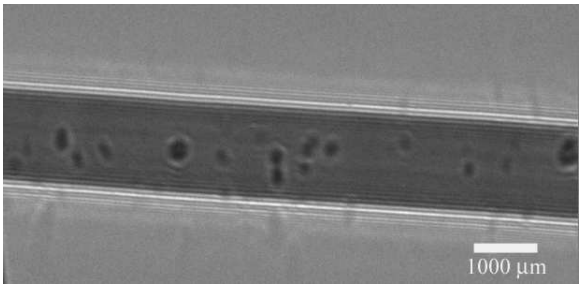

Fig. 12. A background-corrected hologram (contrast image) of a polymer string with $(150 \pm 20)\,\mu$m diameter, supplied by Goodfellow. Source-to-object distance $x_{so} = 1.88$ m, source-to-detector distance $x_{sd} = 13.91$ m, corresponding to a magnification of 7.4 times, tilt angle of the object 46°, X-ray source spot size $\sigma_h = (5.9 \pm 0.1)\,\mu$m, and $\sigma_v = (2.6 \pm 0.1)\,\mu$m, electron beam current 600 nA, exposure time 8.1 s, 50 frames added up.

thickness of 30 μm were taken which were mounted horizontally and vertically. The radiographs are shown in fig. 11. Although the beam size in the horizontal direction $\sigma_h = (1.7 \pm 0.1)\,\mu$m was smaller than $\sigma_v = (3.9 \pm 0.4)\,\mu$m in the vertical direction, no interference patterns were observed for the vertically mounted polymer string. The maximum contrast, $C_{ref} = (I_{max} - I_{min})/(I_{max} + I_{min})$ for the horizontally mounted string was 64%, while for the vertically mounted one it was only 11%. The only reasonable explanation for this observation is that the transverse coherence in the horizontal direction is deteriorated by the monochromator crystal. Obviously, in the energy dispersive direction (horizontally) an additional angular divergence is introduced by the crystal. Since the reason of this effect could not be found, all experiments with strings described in this work were performed with horizontally mounted strings.

Despite the moderate transverse coherence in horizontal direction holograms could be taken which show also interesting features in the horizontal direction. Figure 12 shows a contrast image of a polymer string with a diameter

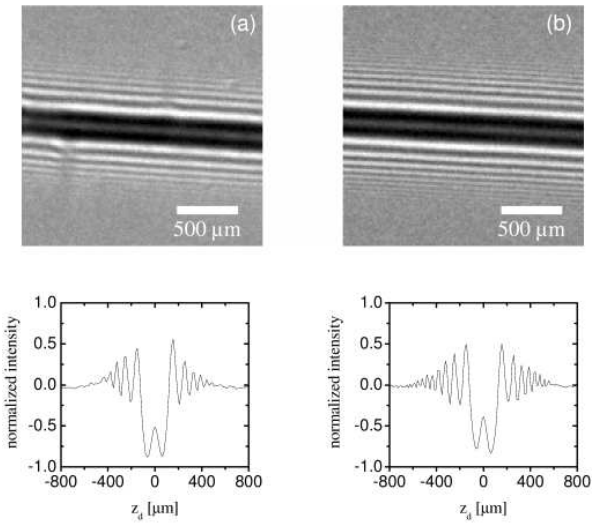

Fig. 13. Fringe visibility as a function of the X-ray source spot size. Shown are holograms of a polymer string with a diameter of 30 μm for an X-ray source spot size as measured with a wire scanner of (a) $\sigma_h = (5.9 \pm 0.1)\,\mu$m, $\sigma_v = (2.6 \pm 0.1)\,\mu$m, and (b) $\sigma_h = (19.1 \pm 0.7)\,\mu$m, $\sigma_v = (0.50 \pm 0.05)\,\mu$m. From the smallest discernible fringe spacings $r_{max} = 50\,\mu$m (a) and 25 μm (b), with eq. (15) standard deviations $\sigma_v = 2.4\,\mu$m (a), and 1.2 μm (b) result. Source-to-object distance $x_{so} = 1.88$ m, object-to-detector distance $x_{od} = 12.03$ m, corresponding to a geometrical magnification of 7.4 times. The angle between string and beam direction amounted to 46°. The electron beam current was 500 nA, exposure time 8.1 s per frame, 100 frames added up.

of $(150 \pm 20)\,\mu$m. According to inspection under an optical microscope the string has a nearly ideal cylindrical shape. No deformations or impurities inside the string could be observed. However, in the hologram inhomogeneities are clearly visible which may be air bubbles or impurity inclusions with a different density than the string material. The background correction assures that these inhomogeneities do not originate from dust particles on the monochromator crystal or the detector.

4.3.2 Optimization of the beam spot size

The most important prerequisite for taking high-quality holograms is the minimization of the beam spot size. In the first step, the spot size was measured with a tungsten wire of $(4.0 \pm 0.4)\,\mu$m diameter which was scanned through the electron beam. In particular, the electrical current of the quadrupole doublet in fig. 9 was varied until the scan yielded the smallest spot size. In the next step holograms of polymer strings were taken with the CCD camera and the spot size was estimated from the smallest discernible fringe visibility estimated according to [25]

$$\sigma = 0.31 \frac{x_{so}}{x_{od}} r_{max}\,. \tag{15}$$

As already mentioned, a CCD chip allows fast on-line imaging, however, the resolution in the direct-exposure

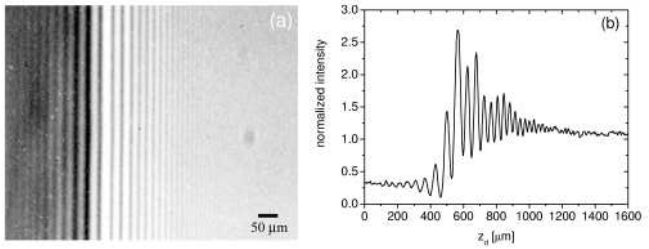

Fig. 14. (a) Hologram of a polyamide string with diameter of $(150 \pm 20)\,\mu$m. Source-to-object distance $x_{so} = 1.88$ m, object-to-detector distance $x_{od} = 11.73$ m, corresponding magnification 7.24 times, X-ray source spot size $\sigma_h = (19.1 \pm 0.7)\,\mu$m and $\sigma_v = (0.50 \pm 0.05)\,\mu$m as measured with the tungsten wire. The X-ray film was digitized with an optical microscope with a magnification of 4 in order to maintain a good resolution. Therefore, only part of the hologram was in the field of view. (b) Intensity profile with 200 rows added up. Notice that also this string was stretched horizontally.

mode is limited by the pixel size of $13\,\mu$m. To achieve a geometrical magnification, the object was placed at close distance to the X-ray source. In fig. 9 the possible positions of the objects are marked. An example of the spot size measurement by the fringe method is shown in fig. 13 which yielded after optimization a standard deviation $\sigma_v = 1.2\,\mu$m.

To exclude a possible influence of the moderate resolution of the CCD detector, high-quality holograms were taken with the high-resolution Structurix D3 X-ray film from Agfa. Figure 14 (a) shows a part of a hologram for a polyamide (Nylon) string. A large number of about 18 interference fringes can be seen, as demonstrated in fig. 14 (b). In this radiograph the main deterioration in the fringe visibility results from the X-ray spot size. The minimum discernible distance between two adjacent fringes is about $25\,\mu$m and the estimated X-ray source size is again about $\sigma_v = 1.2\,\mu$m.

In comparison with the wire scanner measurement which yielded a spot size $\sigma_v = (0.50 \pm 0.05)\,\mu$m, the measured values with the fringe method either determined with the direct exposure CCD, or with the high-resolution X-ray film, deviate significantly. This deviation can be explained by the longitudinal depth of the foil stack which amounts to 2.8 mm. For the measured vertical emittance $\epsilon_v = 0.52\,\mu$m mrad at the electron beam energy of 600 MeV, and a micro-focused electron beam spot size $\sigma_v = (0.50 \pm 0.05)\,\mu$m, the corresponding divergence is 1.04 mrad. When the focus is exactly in the middle of the foil stack, the beam spread within the foil stack amounts to a standard deviation of $1.5\,\mu$m, in accord with the observation with the direct-exposure CCD chip and the X-ray film [4].

4.3.3 Analysis of holograms for polyamide strings

There are two possibilities to analyze holograms of strings. In the first one, calculations on the basis of the Fresnel-

[4] The errors of the fringe method may be in the order of 20%.

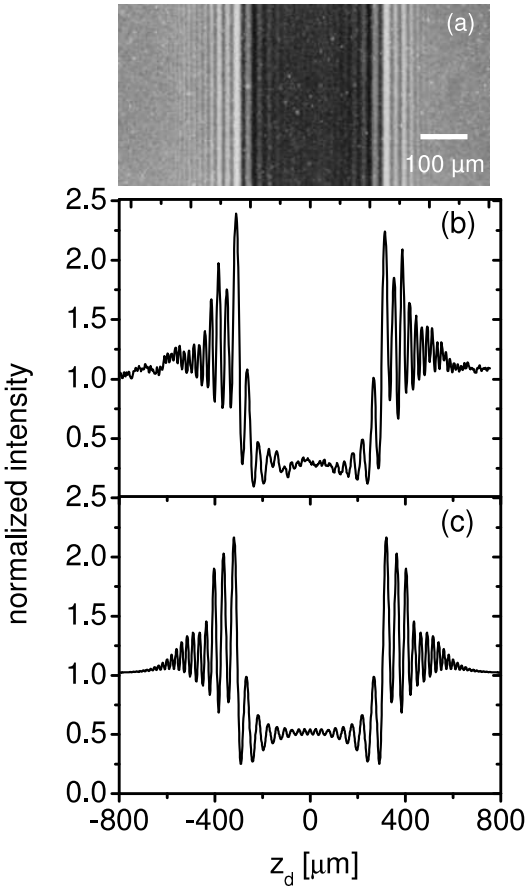

Fig. 15. (a) Radiograph of a polyamide string of $(150 \pm 20)\,\mu$m diameter. Source-to-object distance $x_{so} = 4.3$ m, object-to-detector distance $x_{od} = 9.31$ m, corresponding geometrical magnification 3.17 times, X-ray source size $\sigma_h = (19.1 \pm 0.7)\,\mu$m and $\sigma_v = (0.50 \pm 0.05)\,\mu$m. The X-ray film was digitized with an optical microscope with a magnification of 4. (b) Intensity profile, 200 rows added up. (c) Calculated intensity profile of the radiograph. The spatial resolution of the X-ray source spot size, $\sigma_v = (0.50 \pm 0.05)\,\mu$m, of the film, $\sigma_f = (1.2 \pm 0.4)\,\mu$m, and the optical resolution, $\sigma_{sc,4} = (4.1 \pm 0.1)\,\mu$m, were incorporated in the calculations.

Kirchhoff integrals can be performed in which assumptions about the density and morphology of the string are incorporated. The right solution can be found by a systematical trial and error method. An example is shown in fig. 15. Although a good overall agreement between measurement and calculation could be achieved with the assumption of a homogeneous density distribution within the string, in detail significant differences in the interference pattern close to the boundaries can be recognized. These differences may indicate a density gradient at the periphery of the string. Refinements of the string model are required to further investigate the origin of these differences.

The second possibility is based on reconstruction algorithms to find the phase profile produced by the transparent object. One of these is the modified Gerchberg-Saxton algorithm [26]. It is an iterative method with which the phase information can be found from two holograms taken

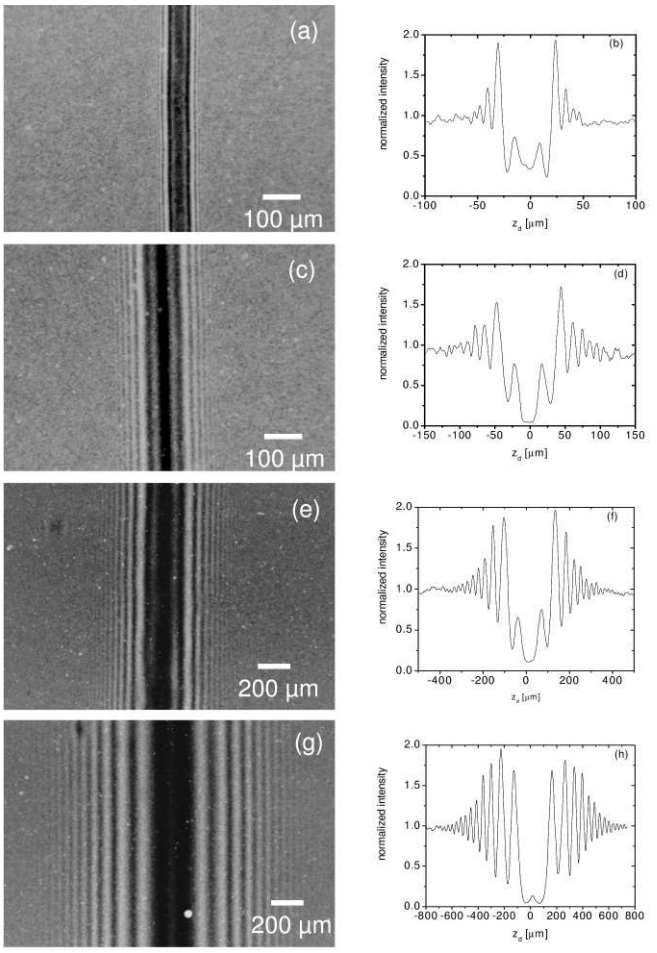

Fig. 16. Holograms of a polyamide string of 30 μm diameter taken at different positions: (a) $x_{od} = 0.9$ m, (c) $x_{od} = 2.83$ m, (d) $x_{od} = 9.31$ m and (g) $x_{od} = 11.73$ m, the latter at an angle of 45°. The corresponding intensity profiles are shown on the right-side in panels (b), (d), (f), and (h), 200 rows were added up. The X-ray film was digitized with an optical microscope, (a) and (b) with a magnification by a factor of 10, (c) and (d) with a magnification by a factor of 4.

at different distances between object and detector. Therefore, holograms of a polyamide string with a diameter of 30 μm were taken at different object-to-detector distances. The holograms are shown in fig. 16.

The selected distances cover different imaging regimes. For the contact regime the contrast would be $(1 - \exp[-(4\pi\beta D)/\lambda]) = 4.26\%$ and the absorption contrast of the polyamide string with a diameter of $D = 30\,\mu$m can be neglected. In the near field region, at an object-to-detector distance $x_{od} = 0.9$ m, fig. 16 (a) and (b), the interference pattern produced by both edges have only very little overlap. The reason is that the size of the first Fresnel zone $\sqrt{\lambda x_{od}} = 13.6\,\mu$m is smaller than the diameter of the string. However, at the largest distance $x_{od} = 11.73$ m, fig. 16 (g) and (h), one obtains for the first Fresnel zone $\sqrt{\lambda x_{od}} = 49.2\,\mu$m and the interference pattern from both edges do overlap. The resemblance between the original object and the radiograph is more or less lost. Both limiting cases may be of particular interest for the reconstruction of the phase profile. However, this issue went beyond the scope of this explorative experimental work and is subject of ongoing investigations.

4.4 Conclusions

Phase contrast radiography has been accomplished with an external 855 MeV electron beam using broad-band transition radiation X-rays with a mean photon energy $\langle\hbar\omega\rangle \approx 20$ keV and a micro-focus with standard deviations of typically $\sigma_h = 8.6\,\mu$m and $\sigma_v = 7.5\,\mu$m in the horizontal and vertical direction, respectively. In-line holograms of polymer strings were taken with a low-emittance 600 MeV electron beam using narrow-band transition radiation X-rays with a photon energy of $\hbar\omega = 6$ keV and a micro-focus with a standard deviation of typically $\sigma_v = 1.2\,\mu$m. High-quality holograms were obtained with high-resolution X-ray films and a direct-exposure cooled CCD camera chip. The advantage of the former is the very good spatial resolution, that of the latter its on-line capability.

An X-ray beam spot with micro-dimensions can be prepared directly with the micro-focused external electron beam via transition radiation production in a foil stack. Objects to be investigated can be placed in close distance to the small X-ray beam spot. This has the advantage that a large geometrical magnification of up to a factor of 10 can easily be achieved in our relatively small experimental area. The disadvantage of the transition radiation X-ray source is its contamination with high-energy bremsstrahlung photons.

Typical electron beam charges required to capture a single image are about 0.3 μC for phase contrast radiographs with broad-band polychromatic X-rays and an X-ray film as detector, and some nC for a cooled CCD chip. In-line holograms with narrow-band X-rays require about 500 μC for a high-resolution X-ray film, and 5–10 μC for the CCD detector.

We thank F. Hagenbuck, and H.-K. Kaiser for significant contributions in the early stage of the experiment, and Mrs. C. Koch-Brandt, Institut für Biochemie, Universität Mainz, for making her film scanner device available to us. This work has been supported by Deutsche Forschungsgemeinschaft DFG under contract BA 1336/1-4.

References

1. F. Arfelli, M. Assante, V. Bonvicini, A. Bravin, G. Cantatore, E. Castelli, L. Dalla Palmaz, M. Di Michiel, R. Longox, A. Olivox, S. Panix, D. Pontoni, P. Poropat, M Prestx, A Rashevskyx, G. Trombay, A. Vacchix, E. Vallazza, F. Zanconati, Phys. Med. Biol. **43**, 2845 (1998).
2. C.J. Kotre, I.P. Birch, Phys. Med. Biol. **44**, 2853 (1999).
3. L.D. Turner, B.B. Dhal, J.P. Hayes, A.P. Mancuso, K.A. Nugent, D. Paterson, R.E. Scholten, C.Q. Tran, A.G. Peele, Opt. Expr. **12**, 2960 (2004).

4. F. Pfeiffer, T. Weitkamp, O. Bunk, Ch. David, Nature Physics —advance online publication— www.nature.com/naturephysics, published online: 26 March 2006; doi:10.1038/nphys265.
5. S.W. Wilkins, T.E. Gureyev, D. Gao, A. Pogany, A.W. Stevenson, Nature (London) **384**, 335 (1996).
6. Xizeng Wu, Hong Liu, Med. Phys. **30**, 2169 (2003).
7. T. Takeda, A. Momose, E. Ueno, Y. Itai, J. Synchrotron Rad. **5**, 1133 (1998).
8. R.A. Lewis, Phys. Med. Biol. **49**, 3573 (2004).
9. D. Gabor, Nature **161**, 777 (1948).
10. P. Spanne, C. Raven, I. Snigireva, A. Snigirev, Phys. Med. Biol. **44**, 741 (1999).
11. P. Cloetens, R. Barrett, J. Baruchel, J. Guigay, M. Schlenker, J. Phys. D **29**, 133 (1996).
12. Z.W. Hu, B. Lai, Y.S. Chu, Z. Cai, D.C. Mancini, B.R. Thomas, A.A. Chernov, Phys. Rev. Lett. **87**, 148101 (2001).
13. R.W. James, *The optical Principles of the Diffraction of X-rays* (Cornell University Press, 1965).
14. V. Kohn, I. Snigireva, A. Snigirev, Opt. Commun. **198**, 293 (2001).
15. Mahmoud El Ghazaly, *X-ray Phase Contrast Imaging at the Mainz Microtron MAMI*, Dissertation, Institut für Kernphysik, Universität Mainz, 2005.
16. B.L. Henke, J.Y. Uejio, G.F. Stone, C.H. Dittmore, F.G. Fujiwara, J. Opt. Soc. Am. B. **11**, 1540 (1986).
17. http://www.filmscanner.info/NikonSuperCoolscan-4000ED.html.
18. Georg Joos, Erwin Schopper, *Grundriss der Photographie und ihrer Anwendungen besonders in der Atomphysik* (Akademische Verlagsgesellschaft M. B. H., Frankfurt am Main, 1958).
19. Y. Hwu, H.H. Hsieh, M.J. Lu, W.L. Tsai, H.M. Lin, W.C. Goh, B. Lai, J.H. Je, C.K. Kim, D.Y. Noh, H.S. Youn, G. Tromba, G. Margaritondo, J. Appl. Phys. **86**, 4613 (1999).
20. O. Chubar, A. Snigirev, S. Kuznetsov, T. Weitkamp, V. Kohn, *Proceedings DIPAC 2001, ESRF, Grenoble, France.*
21. A. Caticha, Phys. Rev. A **40**, 4322 (1989).
22. http://www.andor-tech.com/germany/products/oem.cfm
23. http://www.data.it/support/data_sheets/e2vtech/47-10back.pdf
24. http://www.olympus.pl/pliki/mikroskopy/dokumenty/LM_cameras_ENG.pdf.
25. C. Raven, *Microimaging and Tomography with High Energy Coherent Synchrotron X-Rays* (Shaker Verlag, 1998).
26. R.W. Gerchberg, W.O. Saxton, Optik **35**, 237 (1972).